Geophysical Research Letters

RESEARCH LETTER
10.1029/2018GL081001

Key Points:
- We examine postseismic slip following M4-5 earthquakes using borehole strain data
- The median estimated postseismic moment is between 0.25 and 0.6 times the coseismic moment
- The postseismic moment ratio is intermediate between estimates for small and large earthquakes

Supporting Information:
- Supporting Information S1
- Table S1
- Table S2

Correspondence to:
J. C. Hawthorne,
jessica.hawthorne@earth.ox.ac.uk

Citation:
Alwahedi, M. A., & Hawthorne, J. C. (2019). Intermediate-magnitude postseismic slip follows intermediate-magnitude (M 4 to 5) earthquakes in California. *Geophysical Research Letters*, *46*, 3676–3687. https://doi.org/10.1029/2018GL081001

Received 19 OCT 2018
Accepted 15 MAR 2019
Accepted article online 20 MAR 2019

Intermediate-Magnitude Postseismic Slip Follows Intermediate-Magnitude (M 4 to 5) Earthquakes in California

M. A. Alwahedi[1,2] **and J. C. Hawthorne**[3]

[1]School of Earth and Environment, University of Leeds, Leeds, UK, [2]Now at Institute for Risk and Disaster Reduction, University College London, London, UK, [3]Department of Earth Sciences, University of Oxford, Oxford, UK

Abstract The magnitude of postseismic slip is useful for constraining physical models of fault slip. Here we examine the postseismic slip following intermediate-magnitude (M 4 to 5) earthquakes by systematically analyzing data from borehole strainmeters in central and northern California. We assess the noise in the data and identify 11 earthquakes that generated interpretable strain records. We estimate the earthquakes' postseismic to coseismic moment ratios by comparing the coseismic strain changes with strain changes induced by afterslip in the following 1.5 days. The median estimated postseismic moment is 0.45 times the coseismic moment, with a 90% confidence interval between 0.25 and 0.60. This postseismic moment is slightly larger than typically observed following large ($M > 6$) earthquakes but smaller than observed following small (M2 to 4) earthquakes. The intermediate-magnitude postseismic slip suggests a size dependence in the dynamics of earthquakes or in the properties of fault areas that surround earthquakes.

1. Introduction

Deformation in the hours to years following earthquakes accumulates via a range of processes, including afterslip, poroelastic flow, and viscoelastic deformation. Afterslip is often inferred to cause most of the deformation in the first few hours to months (Amoruso & Crescentini, 2009; Fukuda et al., 2009; Freed, 2007; Ryder et al., 2010). The afterslip that accumulates following large ($M > 6$) earthquakes typically has moment equal to 10% to 30% of the coseismic moment (e.g., Cetin et al., 2012; D'Agostino et al., 2012; Donnellan & Lyzenga, 1998; Gahalaut et al., 2008; Gonzalez-Ortega et al., 2014; Johanson & Bürgmann, 2010; Lin et al., 2013; Segall et al., 2000), though afterslip moments for individual earthquakes range from a few percent to several hundred percent of the coseismic moment (e.g., Bürgmann et al., 2001; Dogan et al., 2014; Freed, 2007; Langbein et al., 2006; Paul et al., 2007).

While afterslip moments vary, the postseismic to coseismic moment ratios estimated for large earthquakes show no systematic trend with magnitude (see Fattahi et al., 2015, Lin et al., 2013, and Figure 4 for summaries). The inferred magnitude-independent afterslip is consistent with a self-similar model of earthquakes, where large earthquakes are scaled versions of smaller ones. However, it has also been proposed that smaller earthquakes have larger afterslip, as such large afterslip could help explain the long recurrence intervals of small repeating earthquakes (Chen & Lapusta, 2009), and geodetic analysis of small (M 1.9 to 3.5) earthquakes near San Juan Bautista, CA, revealed afterslip with moment roughly equal to the coseismic moment, on average (Hawthorne et al., 2016). Those large afterslip moments could simply indicate that the frictional properties of the San Andreas Fault near San Juan Bautista are unusual and more prone to large afterslip. Afterslip with moment 1.5 to 3 times the coseismic moment was identified following several larger earthquakes in the area: the 2004 M 6 Parkfield earthquake (Barbot et al., 2009; Freed, 2007; Langbein et al., 2006), the 2007 M 5.4 Alum Rock earthquake (Murray-Moraleda & Simpson, 2009), and the 1998 M 5.1 San Juan Bautista earthquake (Taira et al., 2014).

But the large afterslip moments identified following $M < 3.5$ earthquakes could also indicate that the self-similar scaling of earthquakes breaks down as earthquakes become smaller. For instance, the afterslip moment could change as earthquake rupture extents become similar to the minimum earthquake nucleation size and thus become too small to drive more rapid slip (Chen & Lapusta, 2009). Alternatively, the afterslip

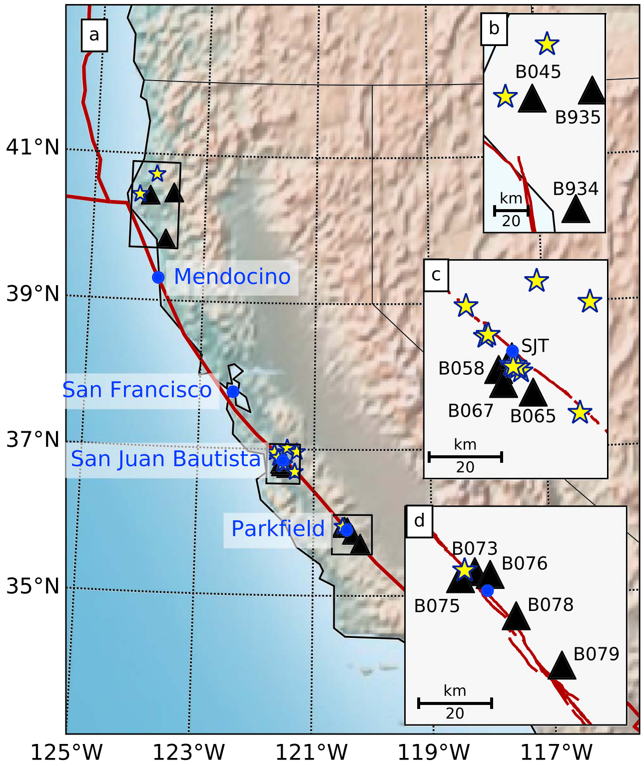

Figure 1. (a) Map of the central San Andreas Fault system in California. In all plots, black triangles are strainmeter locations, yellow stars are the earthquakes for which we estimate postseismic signals, blue circles are cities, and the red lines mark plate boundaries. (b, c, and d) Maps of the three clusters of strainmeters. Note that the marker for SJT is behind the central group of earthquakes in panel c.

moment could increase as earthquake rupture extents become smaller than the seismogenic zone width. $M < 6$ earthquakes may have large afterslip because that afterslip occurs within the seismogenic zone, rather than above and below it.

In this study, we attempt to differentiate between these mechanisms by examining afterslip following intermediate-magnitude (M 4 to 5) earthquakes. Only a few afterslip moments have been estimated for M 4 to 6 earthquakes, and all reported values are large. Afterslip moments between 1 and 6 times the coseismic moment were observed following M 4.7 to 5.5 earthquakes on the Chaman fault (Furuya & Satyabala, 2008), on the Ghazaband fault (Fattahi et al., 2015), near Alum Rock, CA (Murray-Moraleda & Simpson, 2009), and near Mogul, NV (Bell et al., 2012). However, these large afterslip moments could reflect a reporting bias, as smaller amounts of afterslip would be difficult to observe.

Here we use high-precision borehole strain data to examine postseismic slip following M 4 to 5 earthquakes in central and northern California. We systematically identify earthquakes with resolvable coseismic deformation at each of 12 strainmeters in the PBO and USGS networks. We are able to assess the afterslip moment for 11 earthquakes and estimate that the median afterslip moment is 0.45 times the coseismic moment, between the values obtained for smaller and larger earthquakes.

2. Available Data and Earthquakes

We examine data from 12 strainmeters located along the San Andreas Fault in California, shown in Figure 1. More than half of the high-quality earthquake records will come from strainmeter SJT, which was installed by the USGS in 1983 at the northern end of the central creeping section (Gladwin et al., 1987). The remaining records come from strainmeters that were installed by UNAVCO as part of the Plate Boundary Observatory (PBO). We consider data from 11 PBO strainmeters installed between 2006 and 2008. Strainmeters B073, B075, B076, B078, and B079 are located near Parkfield, at the southern edge of the central creeping section, while strainmeters B058, B065, and B067 are located near San Juan Bautista, at the northern edge of the central creeping section, and strainmeters B045, B934, and B935 are located close to the Mendocino triple junction, near another creeping section of the San Andreas.

Small earthquakes occur frequently along these creeping sections, mostly at depths of 4 to 15 km (e.g., Irwin & Barnes, 1975; Waldhauser & Schaff, 2008). We begin our analysis by identifying all M 4 to 6 earthquakes that occurred within 30 km of the strainmeters while the strainmeters were operating, as recorded in the NCSN catalog up until 2017. This identification recovers 112 potential earthquake-station pairs, or 336 potential strain records, as each strainmeter records three components of strain. However, we find in section 5 that only 35 earthquake-station pairs display well-resolved coseismic offsets. Of these 35, only 17 pairs are uncontaminated by creep events or nearby earthquakes, and only 13 pairs, which cover 11 unique earthquakes, have low enough noise level that we can usefully assess the magnitude of postseismic deformation. We describe each step of our data selection and analysis below as well as in Figure S20 in the supporting information.

3. Initial Data Processing: Removing Nontectonic Signals

The deformation produced by coseismic and postseismic slip is recorded at the strainmeters via three to four horizontal extensometers, which are located at depths of 150 to 250 m and measure changes in the horizontal borehole width at various azimuths. SJT records deformation at 18-min intervals, and we use data with 10-min sampling from the PBO strainmeters. We convert the extensometer measurements to estimates of the horizontal components of strain (ϵ_{E+N}, ϵ_{E-N}, and ϵ_{2EN}) using tidal calibrations derived by J. Langbein for strainmeter SJT and by Hodgkinson et al. (2013) for the PBO strainmeters.

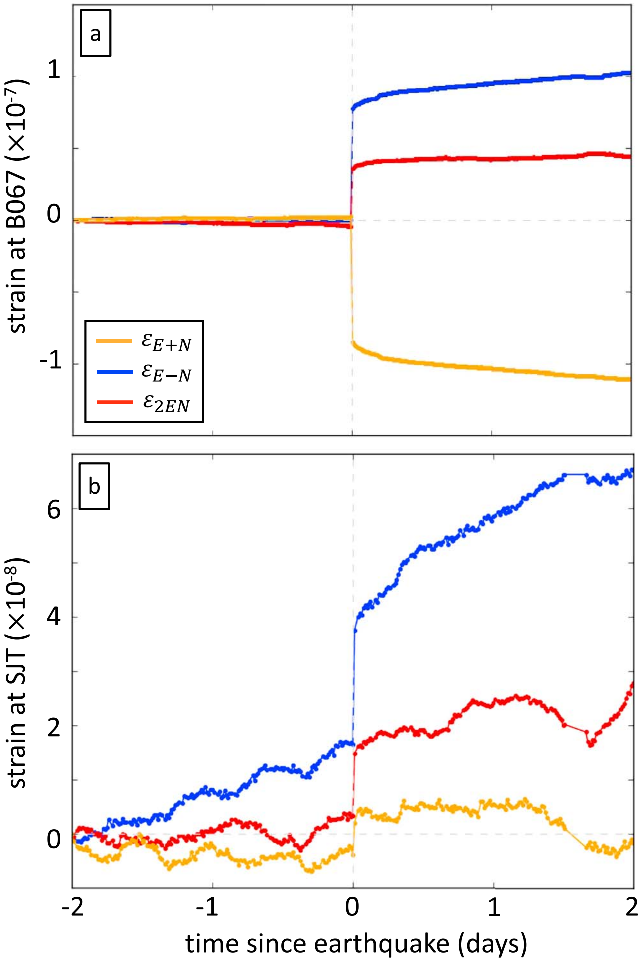

Figure 2. Illustrative records of co- and postseismic strain for (a) a *M* 4.2 earthquake on 20-Nov-2014, recorded at B067 and located 5 km NE of the strainmeter at 6 km depth and (b) a *M* 4.0 earthquake on 11-Feb-2001, recorded at SJT and located 5 km SE of the strainmeter at 6 km depth.

We will directly analyze the time series of ε_{E+N}, ε_{E-N}, and ε_{2EN} recorded at strainmeter SJT. But for the PBO strainmeters, we analyze different linear combinations of these strain components. All the strain components are recorded with high instrumental precision, less than 1 nanostrain, but the various components of strain have different sensitivity to atmospheric and hydrologic noise, so we follow the procedure described by Hawthorne et al. (2016) to identify linear combinations of ε_{E+N}, ε_{E-N}, and ε_{2EN} that are normally less noisy: those that have minimal response to atmospheric pressure variations. We refer to the linear combinations that are closest to the original components as ε_{E+N-na}, ε_{E-N-na}, and ε_{2EN-na}, and we will analyze all three time series at the PBO strainmeters, though we note that only two of these three components are independent. The third component is a linear combination of the first two.

Having isolated the strain components of interest, we estimate and remove several nontectonic signals from each time series following a standard approach (e.g., Hart et al., 1996; Hawthorne et al., 2016; Langbein, 2010; Roeloffs, 2010). To remove borehole curing signals, we discard the first 18 months of data at each station and then fit and remove a linear trend and a decaying exponential with time constant around 1 year. Then we estimate and remove shorter-timescale nontectonic variations. We compare the tidal model of Cartwright and Edden (1973) with the data and identify tidal frequencies that are likely to have signals with amplitudes of at least 0.5 times the noise level. We estimate best-fitting sinusoids at those frequencies and remove them. At SJT, we also estimate and remove a linear response to atmospheric pressure and a periodic 3-hr signal that is likely instrumental noise, as identified by Hawthorne et al. (2016). Further details on this nontectonic correction procedure are given by Hawthorne et al. (2016).

4. Interpreting Strain Records: A Few Examples

After removing these nontectonic signals, we can analyze the earthquake- and afterslip-induced strain. We begin with two examples of the coseismic and postseismic strain, as shown in Figure 2. Additional records are in Figures S1-S17 and S19. Figure 2a shows high-quality records of a *M* 4.2 earthquake located about 5 km NE of strainmeter B067. Figure S22 shows the records in more detail. In both figures, an abrupt coseismic strain step is followed by the gradual accumulation of postseismic strain over the 2 days shown. Figure 2b shows a similar record of a *M* 4.0 earthquake located about 5 km SE of strainmeter SJT, but here the signal-to-noise ratio is lower.

In our modeling, we will assume that the postseismic strain is created by afterslip. If afterslip occurs in an area within 1 to 2 earthquake radii of the earthquake rupture, as is usually observed following large earthquakes (D'Agostino et al., 2012; Ryder et al., 2007), and if the earthquake radius is small relative to the earthquake-strainmeter distance, then the coseismic and postseismic slip should appear colocated from the perspective of the strain observations. In other words, the coseeismic and postseismic slip should have approximately the same Green's functions. Such similar Green's functions are consistent with the data for the earthquakes shown in Figures 2 and S22. The ratio of postseismic to coseismic strain is similar on the three strain components, as is expected if the strains are given by multiplying the coseismic and postseismic moments by the same Green's functions.

In this study, we are interested in the ratio of the postseismic moment to the coseismic moment. If the Green's functions are the same, the moment ratio can be obtained simply by dividing the postseismic strain by the coseismic strain. In Figure 2a, for instance, we may note that the postseismic strains accumulated within 1.5 days of the earthquake have magnitude about 20% of the coseismic strains. Such strain ratios suggest that the afterslip moment accumulated within 1.5 days of the earthquake is about 20% of the coseismic moment.

5. Identifying Interpretable Strain Records

We would like to examine the postseismic and coseismic strain records following as many earthquakes as possible. As a first step, we search for *M* 4 to 5 earthquakes located within 30 km of the strainmeters, and we identify 112 potential earthquake-station pairs. However, most of these records are not interpretable. In our initial culling of the data, we exclude noisy records. We visually examine the 112 records and retain only 35 of them: those where the coseismic offset is well resolved on at least one component. This selection does not bias our analysis toward small postseismic to coseismic moment ratios because the noise in the strain data has a random walk character (Hawthorne & Rubin, 2013; Langbein & Johnson, 1997). The uncertainty in the postseismic strain accumulation, which occurs over a few days, is larger than the uncertainty in the coseismic strain accumulation. For the postseismic strain to be resolvable when the coseismic strain is not, it would have to be about 10 times larger than the coseismic strain.

We do not analyze all records with well-resolved coseismic offsets. Some are too complex to interpret because they clearly include abrupt or large noise signals, occur within earthquake clusters, or trigger creep events. Creep events on the shallow San Andreas Fault are hour- to day-long intervals when part of the fault accelerates to rates of order millimeters to centimeters per hour (Bilham et al., 2004; Gladwin et al., 1994; Schulz et al., 1983; Schulz, 1989; Thurber & Sessions, 1998). In principle, creep events triggered by earthquakes can be classified as afterslip (e.g., Floyd et al., 2016; Fukuda et al., 2009; Langbein et al., 2006). We choose to exclude creep events from our analysis for two reasons. First, it is unclear whether the fault zone processes that create triggered creep events are the same as the processes that usually create afterslip. The spontaneous occurrence of creep events suggests a slip rate-weakening rheology that drives acceleration (e.g., Belardinelli, 1997; Wei et al., 2013) while afterslip is often modeled with a slip rate-strengthening rheology, so that increased slip rates are driven exclusively by the imposed coseismic stress (Helmstetter & Shaw, 2009; Marone et al., 1991; Perfettini & Avouac, 2004).

Second, and more importantly, we exclude creep events because it is difficult to estimate their moments. As noted above, we can estimate the relative moment of afterslip that is located close to the coseismic slip simply by computing the ratio of the postseismic to coseismic strain. But to estimate the relative moment of the triggered creep events, we would need to account for the difference in Green's functions between the coseismic rupture and the creep event slip, and we do not know the creep event locations or the Green's functions well enough to account for that difference. So we identify creep events by (1) looking at the nearby surface USGS creepmeter records and (2) examining how the postseismic to coseismic strain ratio varies among the different components of strain. In the end, we exclude 18 of the 35 earthquake records because of noise, earthquake clusters, and nearby creep events. The excluded earthquakes are listed in Table S2.

6. Estimates of Postseismic Strain

6.1. Primary Analysis

After identifying earthquakes with well-resolved coseismic steps and excluding those with visible creep events, we are left with records from 17 earthquake-station pairs which cover 14 independent earthquakes. We will estimate the coseismic and postseismic strain associated with each of these earthquakes. But first, we estimate and remove a preearthquake linear trend that may result from seasonal or hydrological noise. We estimate the linear trend by dividing the change in strain between 2 days and 5 hr before the earthquake by that time interval (43 hr). This offset-over-time approach to determining offsets and trends is appropriate for the random walk noise that characterizes the strain data (Hawthorne & Rubin, 2013; Langbein & Johnson, 1997).

After removing the preearthquake trend, we estimate the coseismic and postseismic strain changes using each of the three strain components that recorded the earthquake. The coseismic strain change is defined as the strain accumulated within the 40-min interval centered on the earthquake time. Where needed, we linearly interpolate from existing data points to obtain the strain 20 min before and after the earthquakes. The 40-min coseismic interval allows us to identify the entire coseismic strain step from the 10- to 18-min data.

The postseismic strain change is defined as the strain that accumulates between 20 min and 1.5 days after the earthquake. The 1.5-day interval is chosen as a compromise between signal and noise. One and a half days is long enough to allow significant strain signal to accumulate; we seek to examine an interval significantly longer than a few hours because Hawthorne et al. (2016) found that postseismic moment following

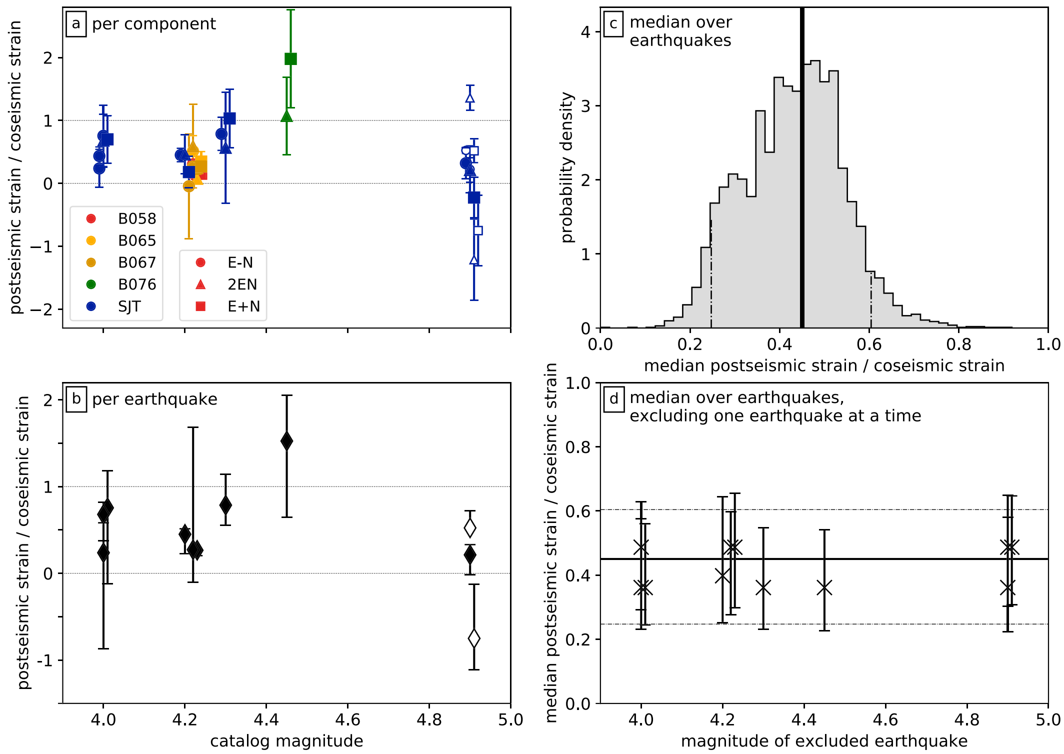

Figure 3. (a) Observed ratios of the postseismic strain changes, from 20 min to 1.5 days after the earthquakes, to the coseismic strain changes, from 20 min before to 20 min after the earthquakes. Each measurement comes from one component at one strainmeter, as indicated by color and symbol. Error bars indicate 70% uncertainty ranges. Note that we randomly shift the magnitudes by up to 0.015 to avoid plotting points on top of each other. (b) Per-earthquake postseismic to coseismic strain ratios with 70% uncertainty ranges, estimated by taking the median of the per-component observations made for each event. (c) Vertical black line: median of the 11 per-earthquake postseismic to coseismic strain ratios plotted in panel b. Shaded gray region: probability distribution for the median postseismic to coseismic strain ratio, obtained by considering various realizations of the noise. Vertical dash-dotted lines delimit 90% confidence intervals. (d) Crosses and error bars: median moment ratios and 90% confidence intervals obtained after excluding one earthquake. The excluded earthquakes' magnitudes are shown on the *x* axis. For comparison, the horizontal solid and dash-dotted lines indicate the median and 90% confidence intervals obtained when including all 11 earthquakes.

$M < 3.5$ earthquakes near strainmeter SJT accumulated relatively slowly in the first 2 to 4 hr before following a log(time) accumulation in the next 1.5 days. We also see accumulation slower than log(time) in the hours following the best-resolved earthquake in our data set (Figure S2). We cannot examine a time interval too much longer than a few hours, however, as the data become more contaminated by atmospheric and hydrologic noise when longer time periods are considered. We choose a 1.5-day postseismic period because it will allow us to analyze well-resolved signals from about 10 earthquakes. We note, however, that significant deformation could accumulate outside of our 1.5-day analysis period. For instance, if postseismic moment accumulates as the logarithm of time t (e.g., Hsu et al., 2006; Perfettini & Avouac, 2004) between 2 hr and 6 months after these earthquakes, 60% of the moment may accumulate after 1.5-days.

We compute the ratios of the 1.5-day postseismic strain to the 20-min coseismic strain on each component and take these ratios as estimates of ratio of the postseismic to coseismic moments. To assess how well resolved each postseismic moment ratio is, we examine how it would change if noise were added. We randomly pick 3,000 4-day-long intervals of the strain time series to use as 3,000 realizations of the noise. We add each realization to the strain data of interest, compute and subtract a preearthquake trend, extract the coseismic and postseismic strain changes, and calculate their ratio. With this approach, we obtain a probability distribution for the moment ratio extracted from each individual strain record. Ratios extracted from the various earthquake, station, and component combinations are plotted in Figure 3a and listed in Table S1. Error bars indicate 70% confidence intervals. Not all of the postseismic moment ratios are plotted, however.

We plot and will further examine only the ratios that have reasonably low uncertainty ranges: those where 70% of the noise-perturbed ratios fall within a range smaller than 2 (e.g., between 0 and 2, or between 0.5 and 2.5). These uncertainty requirements leave us with 33 component-derived ratios, estimated using 13 earthquake-station pairs that cover 11 unique earthquakes. Most of these per-component ratios cluster between 0 and 1.

Simply considering the per-component strain ratios overweights some earthquakes, however: those that are measured on multiple components or strainmeters. So we compute a strain ratio per earthquake by taking the median of the values estimated on the various components and strainmeters. These per-earthquake strain ratios are our best estimates of the earthquakes' postseismic to coseismic moment ratios, and we plot them in Figure 3b. We also estimate probability distributions for the per-earthquake moment ratios by extracting and averaging over sets of values from the per-component probability distributions described in the last paragraph. The error bars in Figure 3b indicate 70% confidence intervals on the per-earthquake moment ratios.

Nine of the 11 best-fitting moment ratios are between 0.2 and 0.8. One earthquake appears to have especially large postseismic slip, with a best-fitting postseismic moment ratio of 1.5, but we should note that its 70% confidence ranges allows values between 0.7 and 2, and given that we estimate postseismic moment ratios for 11 earthquakes, it is likely that the true ratio from at least one moment estimate will fall outside its 90% confidence ranges. It is difficult to resolve variations in postseismic moment among earthquakes with this data set.

It may be more appropriate, then, to focus on estimating the “typical” behavior of these M 4 to 5 earthquakes. Specifically, we note that the median postseismic to coseismic moment ratio is 0.45. To determine the uncertainty on the median ratio, we randomly pick sets of values from the probability distributions for each earthquake. We pick 5,000 sets of ratios and estimate their earthquake-grouped medians. A histogram of the 5,000 ratio estimates is shown in Figure 3c. The probability distribution implies that the median postseismic moment ratio is between 0.31 and 0.54 with 70% probability and between 0.25 and 0.60 with 90% probability.

6.2. Sensitivity to Earthquakes Included

This estimate of the median ratio includes values from two potentially problematic earthquakes, which are marked with open symbols in Figures 3a and 3b. One of the earthquakes, a M 4.9 that occurred in January 1993, displays negative strain ratios on two components, and the 70% confidence interval on the ratio estimated from the third component does not overlap with the ratios of the first two. Such variable strain ratios are inconsistent with afterslip, as afterslip that occurs close to the earthquake should have the same Green's functions as the coseismic slip. The apparently variable ratios observed for this earthquake could simply result from noise, however. These ratios could be 2 σ outliers in the tails of the noise distribution or represent time intervals of especially large hydrologic noise induced by large rainfall in January 1993 (Figures S3 and S18).

Nevertheless, the ratios from this M 4.9 earthquake seem unlikely to represent interpretable postseismic moment estimates, so we consider how excluding this earthquake affects our estimate of the median postseismic moment ratio. The rightmost cross and error bar in Figure 3d show the median moment ratio and 90% error bars obtained after excluding this event. The other symbols indicate the ratios obtained after excluding each of the other 10 earthquakes, one at a time. The median moment ratios differ from the all-event estimate only marginally. They are between 0.36 and 0.49, with 90% confidence intervals that fall between 0.22 and 0.65.

The confidence intervals also change only slightly if we exclude earthquakes whose ratio measurements are inconsistent with afterslip: those where the ratios estimated on individual components differ from the median ratio among components with 70% probability. There are only two such earthquakes: the M 4.9 discussed above and the other M 4.9 marked with open symbols in Figures 3a and 3b, which occurred in April 1996. After excluding these earthquakes, we estimate a median postseismic moment ratio of 0.45 and a 90% confidence interval of 0.25 to 0.67.

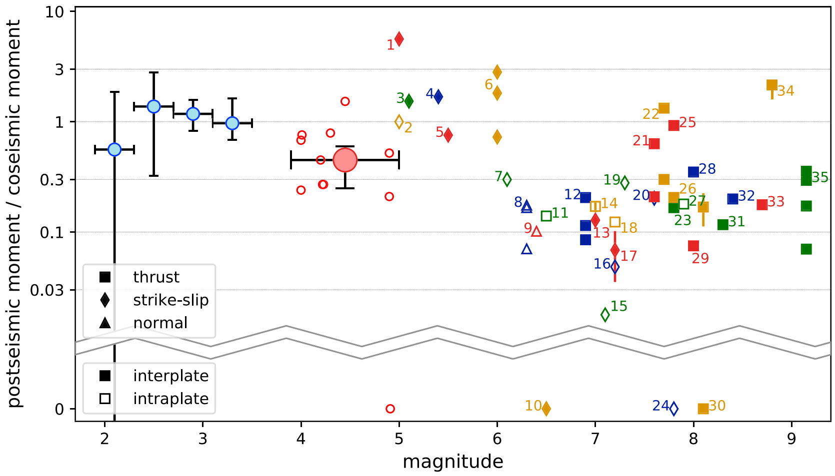

Figure 4. Postseismic to coseismic moment ratios for earthquakes with a range of magnitudes. Note that nonzero values range from 0.02 to 7 and are plotted on a log scale. Zero values are plotted below the break. The small red open circles are the per-earthquake ratios from this study, and the large red circle with error bars is the earthquake-averaged median with 90% uncertainty ranges vertically and the range of magnitudes horizontally. The blue circles with error bars on the left are the moment ratios obtained by Hawthorne et al. (2016) for small earthquakes near San Juan Bautista, again with 90% uncertainty ranges vertically and the range of magnitudes horizontally. The points on the right come from some of the numerous studies of intermediate and large-magnitude earthquakes, mostly made over timescales of days to years. These studies and their observation time intervals are listed and numbered in the text and in Table S3. Note that we sometimes plot multiple postseismic moment estimates for a single earthquake. These estimates come from observations over different time intervals or from different studies and are indicated by points with common color, symbol, and magnitude value.

7. Discussion

7.1. Comparison With Smaller and Larger Earthquakes

The postseismic to coseismic moment ratios estimated in this study are plotted along with the ratios inferred for smaller and larger earthquakes in Figure 4. The postseismic moments for smaller ($M < 3.5$) earthquakes were obtained over the same time interval considered here: from 20 min to 1.5 days after the earthquakes (Hawthorne et al., 2016). The postseismic observations of larger earthquakes were made by a range of researchers over a range of timescales, from days to years after the earthquakes, as listed in Table S3. The large-event moment ratios come from 35 earthquakes numbered in Figure 4, from the 1: 2005 Chaman (Furuya & Satyabala, 2008), 2: 2008 Mogul, NV swarm (Bell et al., 2012), 3: 1998 San Juan Bautista (Taira et al., 2014), 4: 2007 Alum Rock, CA (Murray-Moraleda & Simpson, 2009), 5: 2007 Ghazaband (Fattahi et al., 2015), 6: 2004 Parkfield (Freed, 2007; Langbein et al., 2006), 7: 2014 South Napa (Amoruso & Crescentini, 2009; Cheloni et al., 2010; Floyd et al., 2016), 8: 2009 L'Aquila (D'Agostino et al., 2012), 9: 2008 Nima-Gaize, Tibet (Ryder et al., 2010), 10: 2000 Iceland (Jónsson, 2008), 11: 2003 San Simeon (Johanson & Bürgmann, 2010), 12: 2003 Zemmouri (Cetin et al., 2012; Mahsas et al., 2008), 13: 1989 Loma Prieta (Segall et al., 2000), 14: 1991 Racha, Georgia (Podgorski et al., 2007), 15: 1999 Hector Mine (Jacobs et al., 2002), 16: 2003 Altai (Barbot et al., 2008), 17: 2010 El Mayor-Cucapah (Gonzalez-Ortega et al., 2014), 18: 2011 Van (Dogan et al., 2014), 19: 1992 Landers (Savage & Svarc, 1997), 20: 1997 Manyi, Tibet (Ryder et al., 2007), 21: 2012 Nicoya (Hobbs et al., 2017; Malservisi et al., 2015), 22: 1994 Sanriku (Heki et al., 1997; Melbourne et al., 2002), 23: 2015 Gorkha (Sreejith et al., 2016), 24: 2001 Kokoxili, Tibet (Wen et al., 2012), 25: 1997 Kronotsky (Bürgmann et al., 2001), 26: 2016 Pedernales (Rolandone et al., 2018), 27: 2008 Wenchuan (Diao et al., 2018), 28: 1995 Jalisco (Melbourne et al., 2002), 29: 2003 Tokachi-Oki (Miura et al., 2004), 30: 1995 Antofagasta (Melbourne et al., 2002; Pritchard & Simons, 2006), 31: 2015 Illapel (Shrivastava et al., 2016), 32: 2001 Peru (Melbourne et al., 2002), 33: 2005 Nias (Hsu et al., 2006), 34: 2010 Maule (Lin et al., 2013), and 35: 2004 Sumatra (Chlieh et al., 2007; Subarya et al., 2006).

Most observations of afterslip following large ($M > 6$) earthquakes suggest postseismic to coseismic moment ratios less than 0.3, slightly smaller than the 0.45 median ratio that we estimate for M 4 to 5 earthquakes. The postseismic moments reported for M 5 to 6 earthquakes are larger, between 0.5 and 6. But the high values for M 5 to 6 earthquakes could result from observational bias; smaller postseismic moments may not be reported because they would be harder to observe. More interestingly, then, we note that the postseismic moment ratios estimated for smaller ($M < 3.5$) earthquakes are also slightly larger than the ratios obtained here. The $M < 3.5$ earthquakes have average moment ratios clustered around 1 (Hawthorne et al., 2016) while our median moment ratio has 90% confidence intervals between 0.25 and 0.60.

7.2. Potential Physical Explanations

There are several possible explanations for the observed variation in postseismic moment with magnitude. First, the varying postseismic moments could reflect fault properties. Smaller earthquakes may be more likely to occur on creeping sections of faults, perhaps on asperities surrounded by velocity-strengthening fault sections that are more prone to large postseismic slip (e.g., Rolandone et al., 2018; Vaca et al., 2018). The postseismic moment estimates for $M < 3.5$ earthquakes all come from a single 20-km-wide fault segment near San Juan Bautista, CA, which could have particular properties (Hawthorne et al., 2016). But most of the earthquakes investigated here come from that same fault segment, and half are obtained from measurements on the same strainmeter, SJT (see Figures S1 to S9 for the time series).

Both our and Hawthorne et al., 2016's (2016) moment estimates could be somewhat contaminated by creep events that cause larger-than-expected strain signals: by afterslip occurring far from the seismic rupture, perhaps close to the surface. We have excluded strain signals that are inconsistent with afterslip occurring near the seismic rupture, but given the noise level in the data, we cannot be sure that we have excluded all of the creep event records.

It seems unlikely that other physical processes create much of the postseismic deformation we observe. Significant viscoelastic deformation is usually observed only on timescales much longer than 1.5 days (e.g., Bruhat et al., 2011; Johnson et al., 2009; Pollitz et al., 2006). Poroelastic deformation can accumulate more quickly, but it typically has smaller magnitude, just a few percent of the coseismic deformation (Jónsson et al., 2003; Peltzer et al., 1996; 1998) unless there is a nonlinear near-surface response (e.g., Chia et al., 2001; Manga & Wang, 2007; Quilty & Roeloffs, 1997; Wang et al., 2004) or near-borehole deformation due to shaking (Barbour et al., 2015), and Hawthorne et al. (2016) identified no strong near-surface response to passing seismic waves or to creep events in the San Juan Bautista region or at strainmeter SJT.

Assuming, then, that the postseismic deformation reflects afterslip, the magnitude-dependent moment ratios could reflect the time intervals in which we observe that afterslip. Postseismic moment is often observed and modeled to accumulate as log of the time t since the earthquake, or at a rate of $1/t$ (Çakir et al., 2012; Hsu et al., 2006; Ingleby & Wright, 2017; Perfettini & Avouac, 2004). That decay rate itself does not explain the intermagnitude differences, as the differences persist when we normalize by the log of the observation time interval (Figure S21). But the normalized moments could vary or if we or others observe deformation before the moment starts to accumulate as log(time). The moment accumulation may be slower than log(time) at short times after the earthquake if the slipping region takes time to grow outward from the coseismic rupture (Ariyoshi et al., 2009; Dublanchet et al., 2013a, 2013b; Lui & Lapusta, 2016, Perfettini & Ampuero, 2008) or if the fault takes time to accelerate in response to the coseismic stress increase (Marone et al., 1991; Montési, 2004; Perfettini & Avouac, 2004; Savage, 2007). The intermagnitude differences could also arise if moment does not accumulate logarithmically, but exponentially (e.g., D'Agostino et al., 2012; Savage & Svarc, 1997; Shen et al., 1994), and if the characteristic accumulation interval varies relative to our observation times.

The coseismic rupture geometry can also influence the magnitude of postseismic slip. Small earthquakes tend to be more circular (e.g., Abercrombie, 1995; Gomberg et al., 2016; Scholz, 1982; Shaw, 2013) and thus may have a larger perimeter-to-area ratio and a larger region close to the coseismic rupture that can experience and respond to strong coseismic stress changes (Hawthorne et al., 2016). However, the transition from circular to rectangular ruptures is typically inferred to occur when ruptures first start to span the seismogenic zone, at a magnitude around 6 or 7. We observe a change in postseismic moment between $M < 3.5$ earthquakes and M 4 to 5 earthquakes.

Alternatively, the magnitude-dependent postseismic moments could reflect a more fundamental property of earthquake dynamics. For instance, Chen and Lapusta (2009) identified large postseismic slip in rate and state friction models of earthquakes occurring on small asperities, on patches that were not much wider than the earthquake nucleation size. The large afterslip arose because portions of the potentially unstable asperities did not rupture in the earthquakes and instead slipped via aseismic afterslip.

8. Conclusions

As observations of postseismic slip continue to accumulate, the ratio of postseismic to coseismic moment may become an important constraint on physical models of earthquake rupture. The postseismic moment ratios will complement observations of coseismic stress drops. Coseismic stress drops are usually found to be magnitude independent and suggest that earthquakes are self-similar: that large earthquakes are scaled-up small earthquakes. In this study, we have made observations that appear to contradict self-similarity. The median postseismic moment estimated for the 11 well-resolved M 4 to 5 earthquakes is 0.45 (0.25 to 0.60 with 90% probability). This afterslip moment of these intermediate-magnitude moments is intermediate relative to previous observations; it is slightly larger than is typical of $M > 6$ earthquakes and slightly smaller than observed for $M < 3.5$ earthquakes.

Acknowledgments
Strain and creep data for the San Juan Bautista (SJT) station are provided by the United States Geological Survey and are available at their website (http://earthquake.usgs.gov/monitoring/deformation/data/down-load/table.php). The PBO strain data comes from stations operated by UNAVCO for EarthScope and supported by the National Science Foundation EAR-0350028 and EAR-0732947. It can be obtained via IRIS. The Northern California Seismic Network (NCSN) earthquake catalog is provided by the Northern California Earthquake Data Center and the Berkeley Seismological Laboratory (doi: 10.7932/NCEDC). The plotted fault traces come from the Quaternary fault and fold database, provided by the USGS and the California Geological Survey, and are available at this website (http://earthquake.usgs.gov/hazards/qfaults/). The precipitation data used to interpret some records were provided by the National Oceanic and Atmospheric Administration (NOAA), and were accessed from this site (https://www.ncdc.noaa.gov/cdo-web/). We thank an anonymous reviewer, Falk Amelung, and Editor Gavin Hayes for comments that improved the manuscript. M. A. A. was supported by a scholarship from the National Center of Meteorology in the United Arab Emirates.

References

Abercrombie, R. E. (1995). Earthquake source scaling relationships from −1 to 5 ML using seismograms recorded at 2.5-km depth. *Journal of Geophysical Research*, *100*, 24,015–24,036. https://doi.org/10.1029/95JB02397

Amoruso, A., & Crescentini, L. (2009). Slow diffusive fault slip propagation following the 6 April 2009 L'Aquila earthquake, Italy. *Geophysical Research Letters*, *36*, L24306. https://doi.org/10.1029/2009GL041503

Ariyoshi, K., Hori, T., Ampuero, J.-P., Kaneda, Y., Matsuzawa, T., Hino, R., & Hasegawa, A. (2009). Influence of interaction between small asperities on various types of slow earthquakes in a 3-D simulation for a subduction plate boundary. *Gondwana Research*, *16*(3-4), 534–544. https://doi.org/10.1016/j.gr.2009.03.006

Barbot, S., Fialko, Y., & Bock, Y. (2009). Postseismic deformation due to the M_w 6.0 2004 Parkfield earthquake: Stress-driven creep on a fault with spatially variable rate-and-state friction parameters. *Journal of Geophysical Research*, *114*, B07405. https://doi.org/10.1029/2008JB005748

Barbot, S., Hamiel, Y., & Fialko, Y. (2008). Space geodetic investigation of the coseismic and postseismic deformation due to the 2003 M_w 7.2 Altai earthquake: Implications for the local lithospheric rheology. *Journal Geophysical Research*, *113*, B03403. https://doi.org/10.1029/2007JB005063

Barbour, A. J., Agnew, D. C., & Wyatt, F. K. (2015). Coseismic strains on plate boundary observatory borehole strainmeters in southern California. *Bulletin of the Seismological Society of America*, *105*(1), 431–444. https://doi.org/10.1785/0120140199

Belardinelli, M. E. (1997). Increase of creep interevent intervals: A conceptual model. *Tectonophysics*, *277*(1–3), 99–107. https://doi.org/10.1016/S0040-1951(97)00080-2

Bell, J. W., Amelung, F., & Henry, C. D. (2012). InSAR analysis of the 2008 Reno-Mogul earthquake swarm: Evidence for westward migration of Walker Lane style dextral faulting. *Geophysical Research Letter*, *39*, L18306. https://doi.org/10.1029/2012GL052795

Bilham, R., Suszek, N., & Pinkney, S. (2004). California Creepmeters. *Seismological Research Letters*, *75*(4), 481–492. https://doi.org/10.1785/gssrl.75.4.481

Bruhat, L., Barbot, S., & Avouac, J.-P. (2011). Evidence for postseismic deformation of the lower crust following the 2004 M_w6.0 Parkfield earthquake. *Journal Geophysical Research*, *116*, B08401. https://doi.org/10.1029/2010JB008073

Bürgmann, R., Kogan, M. G., Levin, V. E., Scholz, C. H., King, R. W., & Steblov, G. M. (2001). Rapid aseismic moment release following the 5 December, 1997 Kronotsky, Kamchatka, Earthquake. *Geophysical Research Letter*, *28*(7), 1331–1334. https://doi.org/10.1029/2000GL012350

Çakir, Ziyadin, Ergintav, S., Özener, Haluk, Dogan, U., Akoglu, A. M., Meghraoui, M., & Reilinger, R. (2012). Onset of aseismic creep on major strike-slip faults. *Geology*, *40*(12), 1115–1118. https://doi.org/10.1130/G33522.1

Cartwright, D. E., & Edden, A. C. (1973). Corrected tables of tidal harmonics. *Geophysical Journal International*, *33*(3), 253–264. https://doi.org/10.1111/j.1365-246X.1973.tb03420.x

Cetin, E., Meghraoui, M., Cakir, Z., Akoglu, A. M., Mimouni, O., & Chebbah, M. (2012). Seven years of postseismic deformation following the 2003 M_w Zemmouri earthquake (Algeria) from InSAR time series. *Geophysical Research Letter*, *39*, L10307. https://doi.org/10.1029/2012GL051344

Cheloni, D., D'Agostino, N., D'Anastasio, E., Avallone, A., Mantenuto, S., Giuliani, R., et al. (2010). Coseismic and initial post-seismic slip of the 2009 M_w 6.3 L'Aquila earthquake, Italy, from GPS measurements. *Geophysical Journal International*, *181*(3), 1539–1546. https://doi.org/10.1111/j.1365-246X.2010.04584.x

Chen, T., & Lapusta, N. (2009). Scaling of small repeating earthquakes explained by interaction of seismic and aseismic slip in a rate and state fault model. *Journal Geophysical Research*, *114*, B01311. https://doi.org/10.1029/2008JB005749

Chia, Y., Wang, Y.-S., Chiu, J. J., & Liu, C.-W. (2001). Changes of groundwater level due to the 1999 Chi-Chi earthquake in the Choshui River alluvial fan in Taiwan. *Bulletin of the Seismological Society of America*, *91*(5), 1062–1068. https://doi.org/10.1785/0120000726

Chlieh, M., Avouac, J.-P., Hjorleifsdottir, V., Song, T.-R. A., Ji, C., Sieh, K., et al. (2007). Coseismic slip and afterslip of the great M_w 9.15 Sumatra-Andaman earthquake of 2004. *Bulletin of the Seismological Society of America*, *97*(1A), S152–S173. https://doi.org/10.1785/0120050631

D'Agostino, N., Cheloni, D., Fornaro, G., Giuliani, R., & Reale, D. (2012). Space-time distribution of afterslip following the 2009 L'Aquila earthquake. *Journal of Geophysical Research*, *117*, B02402. https://doi.org/10.1029/2011JB008523

Diao, F., Wang, R., Wang, Y., Xiong, X., & Walter, T. R. (2018). Fault behavior and lower crustal rheology inferred from the first seven years of postseismic GPS data after the 2008 Wenchuan earthquake. *Earth and Planetary Science Letters*, *495*, 202–212. https://doi.org/10.1016/j.epsl.2018.05.020

Dogan, U., Demir, D. Ö., Çakir, Ziyadin, Ergintav, S., Ozener, H., Akoğlu, A. M., et al. (2014). Postseismic deformation following the M_w 7.2, 23 October 2011 Van earthquake (Turkey): Evidence for aseismic fault reactivation. *Geophysical Research Letters*, *41*, 2334–2341. https://doi.org/10.1002/2014GL059291

Donnellan, A., & Lyzenga, G. A. (1998). GPS observations of fault afterslip and up per crustal deformation following the Northridge earthquake. *Journal Geophysical Research*, *103*(B9), 21,285–21,297. https://doi.org/10.1029/98JB01487

Dublanchet, P., Bernard, P., & Favreau, P. (2013a). Creep modulation of Omori law generated by a Coulomb stress perturbation in a 3-D rate-and-state asperity model. *Journal Geophysical Research*, *118*, 4774–4793. https://doi.org/10.1002/jgrb.50311

Dublanchet, P., Bernard, P., & Favreau, P. (2013b). Interactions and triggering in a 3-D rate-and-state asperity model. *Journal of Geophysical Research: Solid Earth*, *118*, 2225–2245. https://doi.org/10.1002/jgrb.50187

Fattahi, H., Amelung, F., Chaussard, E., & Wdowinski, S. (2015). Coseismic and postseismic deformation due to the 2007 *M*5.5 Ghazaband fault earthquake, Balochistan, Pakistan. *Geophysical Research Letters*, *42*, 3305–3312. https://doi.org/10.1002/2015GL063686

Floyd, M. A., Walters, R. J., Elliott, J. R., Funning, G. J., Svarc, J. L., Murray, J. R., et al. (2016). Spatial variations in fault friction related to lithology from rupture and afterslip of the 2014 South Napa, California, earthquake. *Geophysical Research Letters*, *43*, 6808–6816. https://doi.org/10.1002/2016gl069428

Freed, A. M. (2007). Afterslip (and only afterslip) following the 2004 Parkfield, California, earthquake. *Geophysical Research Letters*, *34*, L06312. https://doi.org/10.1029/2006GL029155

Fukuda, J., Johnson, K. M., Larson, K. M., & Miyazaki, S. (2009). Fault friction parameters inferred from the early stages of afterslip following the 2003 Tokachi-oki earthquake. *Journal of Geophysical Research.*, *114*, B04412. https://doi.org/10.1029/2008JB006166

Furuya, M., & Satyabala, S. P. (2008). Slow earthquake in Afghanistan detected by InSAR. *Geophysical Research Letter*, *35*, L06309. https://doi.org/10.1029/2007GL033049

Gahalaut, V. K., Jade, S., Catherine, J. K., Gireesh, R., Ananda, M. B., Kumar, P. D., et al. (2008). GPS measurements of postseismic deformation in the Andaman-Nicobar region following the giant 2004 Sumatra-Andaman earthquake. *Journal Geophysical Research*, *113*, B08401. https://doi.org/10.1029/2007JB005511

Gladwin, M. T., Gwyther, R. L., Hart, R. H. G., & Breckenbridge, K. S. (1994). Measurements of the strain field associated with episodic creep events on the San Andreas fault at San Juan Bautista, California. *Journal of Geophysical Research*, *99*, 4559–4565. https://doi.org/10.1029/93JB02877

Gladwin, M. T., Gwyther, R. L., Hart, R., Francis, M., & Johnston, M. J. S. (1987). Borehole tensor strain measurements in California. *Journal of Geophysical Research*, *92*(B8), 7981–7988. https://doi.org/10.1029/JB092iB08p07981

Gomberg, J., Wech, A., Creager, K., Obara, K., & Agnew, D. (2016). Reconsidering earthquake scaling. *Geophysical Research Letters*, *43*, 6243–6251. https://doi.org/10.1002/2016gl069967

Gonzalez-Ortega, A., Fialko, Y., Sandwell, D., Alejandro, N.-P. F., Fletcher, J., Gonzalez-Garcia, J., et al. (2014). El Mayor-Cucapah (M_w 7.2) earthquake: Early near-field postseismic deformation from InSAR and GPS observations. *Journal Geophysical Research*, *119*, 1482–1497. https://doi.org/10.1002/2013jb010193

Hart, R. H. G., Gladwin, M. T., Gwyther, R. L., Agnew, D. C., & Wyatt, F. K. (1996). Tidal calibration of borehole strain meters: Removing the effects of small-scale inhomogeneity. *Journal Geophysical Research*, *101*(B11), 25,553–25,571. https://doi.org/10.1029/96JB02273

Hawthorne, J. C., Bostock, M. G., Royer, A. A., & Thomas, A. M. (2016). Variations in slow slip moment rate associated with rapid tremor reversals in Cascadia. *Geochemistry, Geophysics, Geosystems*, *17*, 4899–4919. https://doi.org/10.1002/2016GC006489

Hawthorne, J. C., & Rubin, A. M. (2013). Short-time scale correlation between slow slip and tremor in Cascadia. *Journal Geophysical Research: Solid Earth*, *118*, 1316–1329. https://doi.org/10.1002/jgrb.50103

Hawthorne, J. C., Simons, M., & Ampuero, J.-P. (2016). Estimates of aseismic slip associated with small earthquakes near San Juan Bautista, CA. *Journal of Geophysical Research*, *121*, 8254–8275. https://doi.org/10.1002/2016JB013120

Heki, K., Miyazaki, S., & Tsuji, H. (1997). Silent fault slip following an interplate thrust earthquake at the Japan Trench. *Nature*, *386*(6625), 595–598. https://doi.org/10.1038/386595a0

Helmstetter, A., & Shaw, B. E. (2009). Afterslip and aftershocks in the rate-and-state friction law. *Journal Geophysical Research*, *114*, B01308. https://doi.org/10.1029/2007JB005077

Hobbs, T. E., Kyriakopoulos, C., Newman, A. V., Protti, M., & Yao, D. (2017). Large and primarily updip afterslip following the 2012 M_w 7.6 Nicoya, Costa Rica, earthquake. *Journal Geophysical Research*, *122*, 5712–5728. https://doi.org/10.1002/2017JB014035

Hodgkinson, K., Langbein, J., Henderson, B., Mencin, D., & Borsa, A. (2013). Tidal calibration of Plate Boundary Observatory borehole strainmeters. *Journal Geophysical Research*, *118*, 447–458. https://doi.org/10.1029/2012JB009651

Hsu, Y.-J., Simons, M., Avouac, J.-P., Galetzka, J., Sieh, K., Chlieh, M., et al. (2006). Frictional afterslip following the 2005 Nias-Simeulue earthquake, Sumatra. *Science*, *312*(5782), 1921–1926. https://doi.org/10.1126/science.1126960

Ingleby, T., & Wright, T. J. (2017). Omori-like decay of postseismic velocities following continental earthquakes. *Geophysical Research Letters*, *44*, 3119–3130. https://doi.org/10.1002/2017gl072865

Irwin, W. P., & Barnes, I. (1975). Effect of geologic structure and metamorphic fluids on seismic behavior of the San Andreas fault system in central and northern California. *Geology*, *3*(12), 713–716. https://doi.org/10.1130/0091-7613(1975)3h713:EOGSAMi2.0.CO;2

Jacobs, A., Sandwell, D., Fialko, Y., & Sichoix, L. (2002). The 1999 (M_w 7.1) Hector Mine, California, earthquake: Near-field postseismic deformation from ERS interferometry. *Bulletin of the Seismological Society of America*, *92*(4), 1433–1442. https://doi.org/10.1785/0120000908

Johanson, I. A., & Bürgmann, R. (2010). Coseismic and postseismic slip from the 2003 San Simeon earthquake and their effects on backthrust slip and the 2004 Parkfield earthquake. *Journal Geophysical Research*, *115*, B07411. https://doi.org/10.1029/2009JB006599

Johnson, K. M., Bürgmann, R., & Freymueller, J. T. (2009). Coupled afterslip and viscoelastic flow following the 2002 Denali Fault, Alaska earthquake. *Geophysical Journal International*, *176*(3), 670–682. https://doi.org/10.1111/j.1365-246X.2008.04029.x

Jónsson, S. (2008). Importance of post-seismic viscous relaxation in southern Iceland. *Nature Geoscience*, *1*(2), 136–139. https://doi.org/10.1038/ngeo105

Jónsson, S., Segall, P., Pedersen, R., & Björnsson, G. (2003). Post-earthquake ground movements correlated to pore-pressure transients. *Nature*, *424*(6945), 179–183. https://doi.org/10.1038/nature01776

Langbein, J. (2010). Computer algorithm for analyzing and processing borehole strainmeter data. *Computers & Geosciences*, *36*(5), 611–619. https://doi.org/10.1016/j.cageo.2009.08.011

Langbein, J., & Johnson, H. (1997). Correlated errors in geodetic time series: Implications for time-dependent deformation. *Journal Geophysical Research*, *102*(B1), 591–603. https://doi.org/10.1029/96JB02945

Langbein, J., Murray, J. R., & Snyder, H. A. (2006). Coseismic and initial postseismic deformation from the 2004 Parkfield, California, earthquake, observed by global positioning system, electronic distance meter, creepmeters, and borehole strainmeters. *Bulletin of the Seismological Society of America*, *96*(4B), S304–S320. https://doi.org/10.1785/0120050823

Lin, Y.-n. N., Sladen, A., Ortega-Culaciati, F., Simons, M., Avouac, J.-P., Fielding, E. J., et al. (2013). Coseismic and postseismic slip associated with the 2010 Maule Earthquake, Chile: Characterizing the Arauco Peninsula barrier effect. *Journal Geophysical Research*, *118*, 3142–3159. https://doi.org/10.1002/jgrb.50207

Lui, S. K. Y., & Lapusta, N. (2016). Repeating microearthquake sequences interact predominantly through postseismic slip. *Nature Communications*, *7*, 1–7. https://doi.org/10.1038/ncomms13020

Mahsas, A., Lammali, K., Yelles, K., Calais, E., Freed, A. M., & Briole, P. (2008). Shallow afterslip following the 2003 May 21, $M_w = 6.9$ Boumerdes earthquake, Algeria. *Geophysical Journal International*, *172*(1), 155–166. https://doi.org/10.1111/j.1365-246X.2007.03594.x

Malservisi, R., Schwartz, S. Y., Voss, N., Protti, M., Gonzalez, V., Dixon, T. H., et al. (2015). Multiscale postseismic behavior on a megathrust: The 2012 Nicoya earthquake, Costa Rica. *Geochemistry, Geophysics, Geosystems*, *16*, 1848–1864. https://doi.org/10.1002/2015GC005794

Manga, M., & Wang, C.-Y. (2007). Earthquake hydrology, *Treatise on geophysics* (Vol. 4, pp. 6054). Amsterdam: Elsevier. Earthquake Seismology.

Marone, C. J., Scholtz, C. H., & Bilham, R. (1991). On the mechanics of earthquake afterslip. *Journal Geophysical Research*, *96*(B5), 8441–8452. https://doi.org/10.1029/91JB00275

Melbourne, T. I., Webb, F. H., Stock, J. M., & Reigber, C. (2002). Rapid postseismic transients in subduction zones from continuous GPS. *Journal Geophysical Research*, *107*(B10), 2241. https://doi.org/10.1029/2001JB000555

Miura, S., Suwa, Y., Hasegawa, A., & Nishimura, T. (2004). The 2003 *M*8.0 Tokachi-Oki earthquake –How much has the great event paid back slip debts? *Geophysical Research Letters*, *31*, L05613. https://doi.org/10.1029/2003GL019021

Montési, L. G. J. (2004). Controls of shear zone rheology and tectonic loading on postseismic creep. *Journal Geophysical Research*, *109*, B10404. https://doi.org/10.1029/2003JB002925

Murray-Moraleda, J. R., & Simpson, R. W. (2009). Geodetically inferred coseismic and postseismic slip due to the *M* 5.4 31 October 2007 Alum Rock earthquake. *Bulletin of the Seismological Society of America*, *99*(5), 2784–2800. https://doi.org/10.1785/0120090017

Paul, J., Lowry, A. R, Bilham, R., Sen, S., & Smalley, R. (2007). Postseismic deformation of the Andaman Islands following the 26 December, 2004 Great Sumatra-Andaman earthquake. *Geophysical Research Letters*, *34*, L19309. https://doi.org/10.1029/2007GL031024

Peltzer, G., Rosen, P., Rogez, F., & Hudnut, K. (1996). Postseismic rebound in fault step-overs caused by pore fluid flow. *Science*, *273*(5279), 1202–1204. https://doi.org/10.1126/science.273.5279.1202

Peltzer, G., Rosen, P., Rogez, F., & Hudnut, K. (1998). Poroelastic rebound along the Landers 1992 earthquake surface rupture. *Journal Geophysical Research*, *103*(B12), 30,131–30,145. https://doi.org/10.1029/98JB02302

Perfettini, H., & Ampuero, J. P. (2008). Dynamics of a velocity strengthening fault region: Implications for slow earthquakes and postseismic slip. *Journal Geophysical Research*, *113*, B09411. https://doi.org/10.1029/2007JB005398

Perfettini, H., & Avouac, J. P. (2004). Postseismic relaxation driven by brittle creep: A possible mechanism to reconcile geodetic measurements and the decay rate of aftershocks, application to the Chi-Chi earthquake, Taiwan. *Journal Geophysical Research*, *109*, B02304. https://doi.org/10.1029/2003JB002488

Podgorski, J., Hearn, E. H., McClusky, S., Reilinger, R., Taymaz, T., Tan, O., et al. (2007). Postseismic deformation following the 1991 Racha, Georgia, earthquake. *Geophysical Research Letters*, *34*, L04310. https://doi.org/10.1029/2006GL028477

Pollitz, F. F, Banerjee, P., Burgmann, R., Hashimoto, M., & Choosakul, N. (2006). Stress changes along the Sunda trench following the 26 December 2004 Sumatra-Andaman and 28 March 2005 Nias earthquakes. *Geophysical Research Letters*, *33*, L06309. https://doi.org/10.1029/2005GL024558

Pritchard, M. E., & Simons, M. (2006). An aseismic slip pulse in northern Chile and along-strike variations in seismogenic behavior. *Journal Geophysical Research*, *111*, B08405. https://doi.org/10.1029/2006JB004258

Quilty, E. G., & Roeloffs, E. A. (1997). Water-level changes in response to the 20 December 1994 earthquake near Parkfield, California. *Bulletin of the Seismological Society of America*, *87*(2), 310–317.

Roeloffs, E. (2010). Tidal calibration of Plate Boundary Observatory borehole strainmeters: Roles of vertical and shear coupling. *Journal Geophysical Research*, *115*, B06405. https://doi.org/10.1029/2009JB006407

Rolandone, F., Nocquet, J.-M., Mothes, P. A., Jarrin, P., Vallée, M., Cubas, N., et al. (2018). Areas prone to slow slip events impede earthquake rupture propagation and promote afterslip. *Science Advances*, *4*(1), eaao6596. https://doi.org/10.1126/sciadv.aao6596

Ryder, I., Bürgmann, R., & Sun, J. (2010). Tandem afterslip on connected fault planes following the 2008 Nima-Gaize (Tibet) earthquake. *Journal Geophysical Research*, *115*, B03404. https://doi.org/10.1029/2009JB006423

Ryder, I., Parsons, B., Wright, T. J., & Funning, G. J. (2007). Post-seismic motion following the 1997 Manyi (Tibet) earthquake: InSAR observations and modelling. *Geophysical Journal International*, *169*(3), 1009–1027. https://doi.org/10.1111/j.1365-246X.2006.03312.x

Savage, J. C. (2007). Postseismic relaxation associated with transient creep rheology. *Journal Geophysical Research*, *112*, B05412. https://doi.org/10.1029/2006JB004688

Savage, J. C., & Svarc, J. L. (1997). Postseismic deformation associated with the 1992 M_w 7.3 Landers earthquake, southern California. *Journal Geophysical Research*, *102*(B4), 7565–7577. https://doi.org/10.1029/97JB00210

Scholz, C. H. (1982). Scaling laws for large earthquakes: Consequences for physical models. *Bulletin of the Seismological Society of America*, *72*(1), 1–14.

Schulz, S. S. (1989). Catalog of creepmeter measurements in California from 1966 through 1988 (*USGS Open-File Report(89-650), 196, (Version 1.1)*). https://doi.org/10.3133/ofr89650

Schulz, S., Burford, R. O., & Mavko, B. (1983). Influence of seismicity and rainfall on episodic creep on the San Andreas fault system in central California. *Journal Geophysical Research*, *88*(B9), 7475–7484. https://doi.org/10.1029/JB088iB09p07475

Segall, P., Bürgmann, R., & Matthews, M. (2000). Time-dependent triggered afterslip following the 1989 Loma Prieta earthquake. *Journal Geophysical Research*, *105*(B3), 5615–5634. https://doi.org/10.1029/1999JB900352

Shaw, B. E. (2013). Earthquake surface slip-length data is fit by constant stress drop and is useful for seismic hazard analysis. *Bulletin of the Seismological Society of America*, *103*(2A), 876–893. https://doi.org/10.1785/0120110258

Shen, Z.-K., Jackson, D. D., Feng, Y., Cline, M., Kim, M., Fang, P., & Bock, Y. (1994). Postseismic deformation following the Landers earthquake, California, 28 June 1992. *Bulletin of the Seismological Society of America*, *84*(3), 780–791.

Shrivastava, M. N., González, G., Moreno, M., Chlieh, M., Salazar, P., Reddy, C. D., et al. (2016). Coseismic slip and afterslip of the 2015 M_w 8.3 Illapel (Chile) earthquake determined from continuous GPS data. *Geophysical Research Letters*, *43*, 10,710–10,719. https://doi.org/10.1002/2016GL070684

Sreejith, K. M., Sunil, P. S., Agrawal, R., Saji, A. P., Ramesh, D. S., & Rajawat, A. S. (2016). Coseismic and early postseismic deformation due to the 25 April 2015, M_w 7.8 Gorkha, Nepal, earthquake from InSAR and GPS measurements. *Geophysical Research Letters*, *43*, 3160–3168. https://doi.org/10.1002/2016GL067907

Subarya, C., Chlieh, M., Prawirodirdjo, L., Avouac, J. P, Bock, Y., Sieh, K., et al. (2006). Plate-boundary deformation associated with the great Sumatra-Andaman earthquake. *Nature*, *440*(7080), 46–51. https://doi.org/10.1038/nature04522

Taira, T., Bürgmann, R., Nadeau, R. M., & Dreger, D. S. (2014). Variability of fault slip behavior along the San Andreas Fault in the San Juan Bautista Region. *Journal Geophysical Research*, *119*, 8827–8844. https://doi.org/10.1002/2014JB011427

Thurber, C., & Sessions, R. (1998). Assessment of creep events as potential earthquake precursors: Application to the creeping section of the San Andreas Fault, California. *Pure and Applied Geophysics*, *152*, 685–705. https://doi.org/10.1007/s000240050172

Vaca, S., Vallée, M., Nocquet, J.-M., Battaglia, J., & Régnier, M. (2018). Recurrent slow slip events as a barrier to the northward rupture propagation of the 2016 Pedernales earthquake (Central Ecuador). *Tectonophysics*, *724-725*, 80–92. https://doi.org/10.1016/j.tecto.2017.12.012

Waldhauser, F., & Schaff, D. P. (2008). Large-scale relocation of two decades of Northern California seismicity using cross-correlation and double-difference methods. *Journal Geophysical Research*, *113*, B08311. https://doi.org/10.1029/2007JB005479

Wang, C.-y., Wang, C.-H., & Manga, M. (2004). Coseismic release of water from mountains: Evidence from the 1999 ($M_w = 7.5$) Chi-Chi, Taiwan, earthquake. *Geology*, *32*(9), 769–772. https://doi.org/10.1130/G20753.1

Wei, M., Kaneko, Y., Liu, Y., & McGuire, J. J. (2013). Episodic fault creep events in California controlled by shallow frictional heterogeneity. *Nature Geoscience*, *6*(7), 566–570. https://doi.org/10.1038/ngeo1835

Wen, Y., Li, Z., Xu, C., Ryder, I., & Bürgmann, R. (2012). Postseismic motion after the 2001 M_w 7.8 Kokoxili earthquake in Tibet observed by InSAR time series. *Journal Geophysical Research*, *117*, B08405. https://doi.org/10.1029/2011JB009043